ES Energy & Environment

COMMUNICATION View Article Online

Experimental and Theoretical Study on Well-Tunable Metal Oxide Doping towards High-Performance Thermoelectrics

Enzheng Shi,[1,2#] Tianli Feng,[3#] Je-Hyeong Bahk,[4] Yu Pan,[5,6] Wei Zheng,[1] Zhe Li,[1] G. Jeffery Snyder,[6] Sokrates T. Pantelides[3] and Yue Wu[1,2*]

Most existing thermoelectric materials exhibit high performance only within a narrow temperature window. Among them, bismuth antimony telluride (BiSbTe) is a typical p-type thermoelectric material working near room temperature, but its performance decays rapidly with increasing temperature mainly due to the bipolar thermal transport. Suppressing bipolar thermal transport normally requires a delicate manipulation of band structure, possibly achievable through well-engineered extrinsic doping. Here we present a straightforward approach to dope BiSbTe with earth-abundant CuO. Different from embedding CuO nanoparticles that were extensively reported in literature, we observed that Cu and O atoms dissociate after spark plasma sintering. Density-functional-theory calculations reveal that it is the substitutional Cu at Sb/Bi sites and the interstitial O impurities that induce holes and increase carrier concentration as well as the power factor. The increase of hole concentration strongly suppresses the bipolar thermal conductivity. To the best of our knowledge, this is the first theoretical demonstration of p-doping of bismuth telluride thermoelelctrics from oxygen. Meanwhile, the Cu defects and O impurities strongly suppress the lattice thermal conductivity. As a result, the obtained material possesses optimized zT over a much wider temperature range with well-controllable peak temperature as a function of CuO concentration.

Keywords: Bismuth antimony telluride, Copper oxide, P-doping, Thermal conductivity

Received 30 September 2018**, Accepted** 13 November 2018

DOI: 10.30919/esee8c182

Thermoelectric (TE) materials can convert waste heat into electricity as well as realize solid-state cooling. The performance of TE materials is evaluated by a dimensionless figure of merit zT, which is defined as $zT=\sigma S^2T/\kappa_{tot}$, where σ is the electrical conductivity, S is the Seebeck coefficient, T is the absolute temperature, and κ_{tot} is the total thermal conductivity. The κ_{tot} is the sum of unipolar electronic κ_e, lattice κ_{lat}, and bipolar κ_{bi}. Many materials with high zT values are under investigation. However, most of these materials possess high zT values only within a very narrow temperature range, which significantly limits potential applications by the obligation to stack multiple materials either in parallel or in series to cover a wide temperature range. Inter-diffusion, thermal interface resistance, and thermal expansion stress reduce the reliability of the TE system. Using bismuth telluride (Bi_2Te_3)-based materials as examples, they are among the best and most widely explored TE materials near room temperature.[1-3] The modulation of the thermoelectric performance of Bi_2Te_3-based materials can be realized by defect engineering and band tailoring methods.[4-9] For example, phonon engineering is the primary strategy to control the lattice thermal conductivity.[10-12] To suppress the pronounced bipolar effect in Bi_2Te_3-based materials at elevated temperatures, extrinsic doping (using metal elements, metal telluride and selenide, Bi or Sb halide) can be adopted to adjust the Fermi level to tune the carrier concentration, thereby effecting the σ, S and κ_{tot}.[13-18] Moreover, as one important class of thermoelectric materials, metal oxides have also drawn significant attention.[19-22] However, compared with Bi_2Te_3-based materials, oxide thermoelectric materials have lower carrier mobilities, higher κ_{lat}, and larger bandgaps, restricting their zT values far below 1.0, while peaking at relatively high temperatures.[19,20] To the best of our knowledge, the application of metal-oxide doping in the Bi_2Te_3-based materials, which may result in a boost of the thermoelectric performance, has never been explored, although it was reported that metal oxide nanopowders could be embedded as nanoinclusions to improve the thermoelectric performance.[23-25]

Indeed, many controversial mechanisms of Cu doping in Bi_2Te_3-based materials have been reported in the past,[13,26-28] as most of them claimed Cu as a p-type dopant yet a few claimed it n-type. While Cu doping remains unclear, O doping in these materials has never been reported yet and the mechanism is unknown. The possibility that Cu impurities are good p-type dopants, i.e., they introduce excess holes in Bi_2Te_3-based materials, has been invoked in the past on the grounds that Cu substitutes Bi^{3+} or Sb^{3+} in a +2 oxidation state.[13] Such arguments,

[1]*Department of Chemical and Biological Engineering, Iowa State University, Ames, IA 50011, USA*
[2]*Ames Laboratory, Department of Energy, Ames, IA 50011, USA*
[3]*Department of Physics and Astronomy and Department of Electrical Engineering and Computer Science, Vanderbilt University, Nashville, TN 37235, USA*
[4]*Department of Mechanical and Materials Engineering, University of Cincinnati, Cincinnati, OH 45221, USA*
[5]*State Key Laboratory of New Ceramics and Fine Processing, School of Materials Science and Engineering, Tsinghua University, Beijing 100084, P. R. China*
[6]*Department of Materials Science and Engineering, Northwestern University, Evanston, IL 60208, USA*
***E-mail:** yuewu@iastate.edu. #These authors contributed equally*

however, have a high degree of uncertainty for impurities that do not come from a column to the immediate left of the host-atom column in the periodic table because there is a substantial likelihood that the defect potential is strong and introduces deep localized levels in the energy gap. To complicate matters further, Bi_2Te_3-based materials have very small energy gaps so that experience from conventional semiconductors, which typically have larger energy gaps, does not provide adequate guidance. No direct experimental evidence or theoretical calculations have been reported so far in support of Cu being a p-type or n-type dopant in Bi_2Te_3-based materials. Oxygen obviously is isoelectronic with Te so that it is not expected to dope either n-type or p-type, if it substitutes one of these two elements. Again, the very small energy gap and the strength of the oxygen potential disallow any definitive conclusions from general considerations.

In this work, we demonstrate a new approach to dope BiSbTe by earth abundant CuO and find that CuO dissociates with Cu dopants tending to partially segregate and O dopants remaining dispersed. CuO of as low as 0.05 %~0.3 % concentration shows an unambiguous p-type doping effect which increases the electrical conductivity and significantly suppresses the bipolar effect, yielding a comprehensively pronounced *zT* (above 1.0) functioning from 313 K to 514 K compared with the pure BiSbTe counterpart. In addition, an excellent controllability of the *zT* peak temperature by varying the CuO concentration demonstrates the capability of the doped BiSbTe materials in a wide temperature range. Boltzmann-transport-equation (BTE) and first-principles density-functional-theory (DFT) modeling are performed to evaluate the contributions from grain size and CuO concentration and to identify the p-type doping from both Cu and O. Specifically, we demonstrate that substitutional Cu at both Sb and Bi sites and interstitial oxygen act as p-type dopants.

Fine commercial $Bi_{0.5}Sb_{1.5}Te_3$ powders (400 mesh, American Elements) were mixed with CuO nanopowders (<50 nm, Sigma Aldrich), followed by a ball-milling process, resulting in a uniform mixture of BiSbTe and x%CuO (x% represents the weight ratio of CuO in the composite). As shown in Fig. 1a, the BiSbTe·x%CuO powders were loaded into a graphite die (Φ=10.5 mm) and sealed by two punches so that the

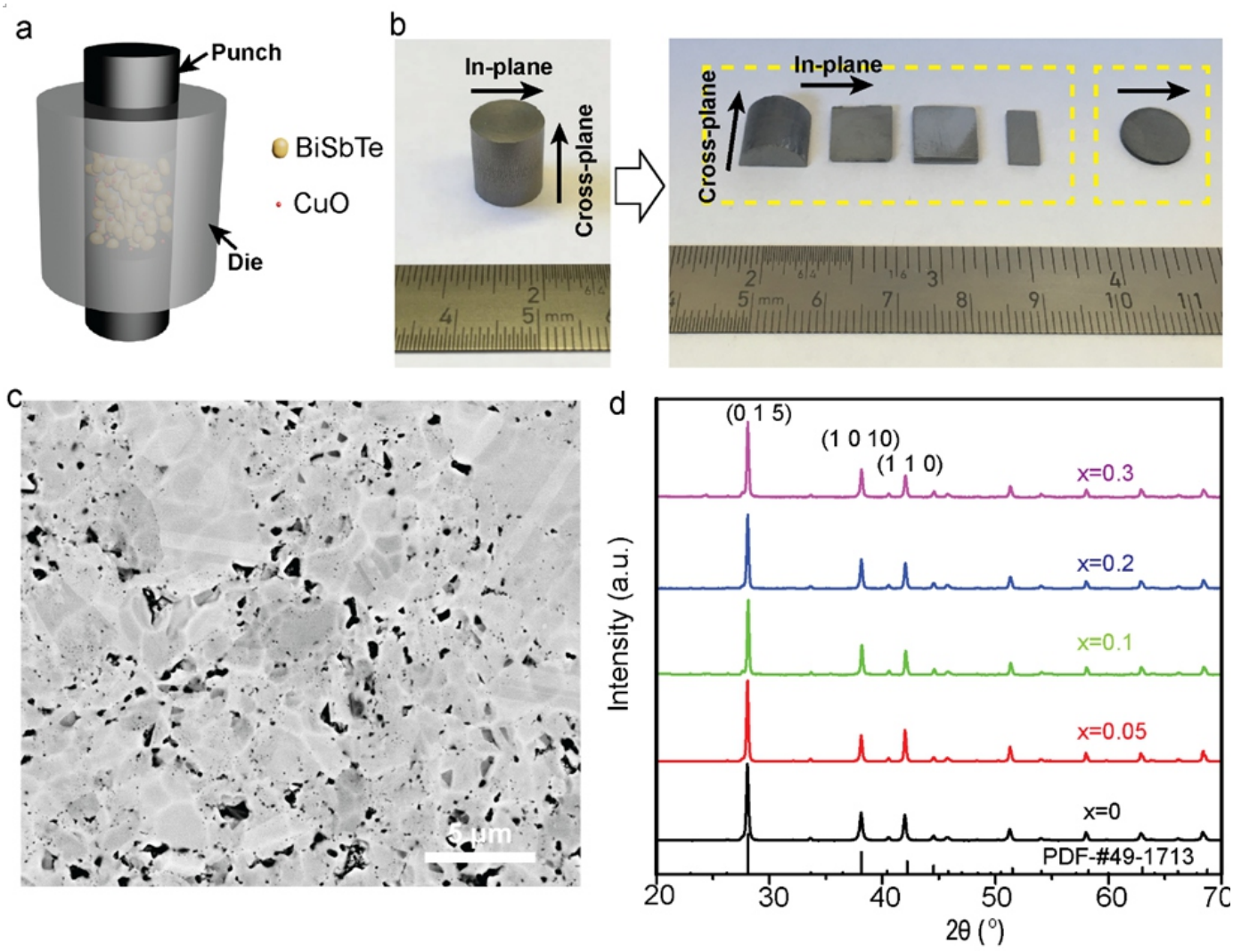

Fig. 1 Characterization of BiSbTe·x%CuO composites. (a) Schematic image of loading the mixture of BiSbTe powder and CuO nanoparticles into graphite die and punches for SPS; (b) Photo images of BiSbTe·x%CuO composites; the left image represents the as-sintered cylindrical sample and the right one corresponds the disk and bars cut from the left tall cylinder; (c) Back-scattering SEM image of BiSbTe·0.3%CuO sample; (d) XRD patterns of BiSbTe·x%CuO composites; The peaks are well matched with the standard hexagonal single phase $Bi_{0.5}Sb_{1.5}Te_3$ (PDF-#49-1713 represents standard $Bi_{0.5}Sb_{1.5}Te_3$ phase).

pressure could be exerted uniaxially. After spark plasma sintering(SPS), a cylinder sample with a height of ~12 mm (the left photo image in Fig. 1b) was obtained. The density of the as-sintered composites was determined to be around 6.70~6.73 g/cm^3, 97.4 %~97.8 % of the theoretical value. To measure the thermoelectric properties along the in-plane and cross-plane directions respectively, the BiSbTe·x%CuO cylinder was diced into several parts (Fig. 1b). The left parts (labeled by the wide dashed yellow rectangle) were used to measure the cross-plane electrical conductivity (σ), Seebeck coefficient (S) and in-plane thermal conductivity (κ_{tot}), while the right disk was used to measure the in-plane σ, S and cross-plane κ_{tot}. All the following thermoelectric properties and characterizations discussed in the main text are along cross-plane direction. The in-plane thermoelectric properties were found to have similar thermoelectric performance as shown in Fig. S1. From the scanning electron microscopy (SEM, Fig. 1c and Fig. S2) images of BiSbTe·0.3%CuO and BiSbTe samples, plenty of tiny pores are included in the composite. And the grain size ranges from tens of nanometers to several micrometers, consistent with the TEM images (Fig. S3). The hierarchical architecture with broad grain size distribution as well as the nanosized pores helps suppress the lattice thermal conductivity due to scattering phonons of different frequencies.[29-31] The matrix phase was identified as $Bi_{0.5}Sb_{1.5}Te_3$ (PDF-#49-1713) according to the X-ray diffraction (XRD) patterns (Fig. 1d). Due to the low CuO concentration (0.05 % to 0.3 %), no secondary phase was recognized from the XRD patterns.

After the SPS process, the thermoelectric properties of BiSbTe ·x%CuO composites were measured. Fig. 2 demonstrates the temperature-dependent electrical conductivity, Seebeck coefficient, and power factor of BiSbTe·x%CuO composites with different CuO concentrations x%. We performed carrier transport modeling based on the linearized Boltzmann transport equation to fit the experimental data and added the fitting curves in Fig. 2. The theoretical model shows an excellent fitting with the experimental data. Detailed information about the modeling can be found in the Supplemental Information (Part 3.1) and Ref.[32] As shown in Fig. 2a, with the increase of CuO concentration x%, σ increases fourfold from 0.32×10^5 S/m (pure BiSbTe) to 1.63×10^5 S/m (BiSbTe·0.3%CuO) at 317 K, implying an effective doping by CuO incorporation. For pure BiSbTe samples, there is a continuous decrease of σ when measured from 300 K to 436 K, which is a typical characteristic of degenerate semiconductors, in which the carrier concentration remains constant and the mobility decreases with temperature due to increased phonon scattering. However, σ begins to increase after the temperature exceeds 436 K for pure BiSbTe, due to the increased minority carriers (bipolar effect). In comparison, the bipolar effect for the BiSbTe·x%CuO composites is effectively suppressed and σ decreases monotonically over the entire measurement temperature range (from 300 to 520 K).

The positive Seebeck coefficient S indicates that the BiSbTe·x%CuO composites are p-type semiconductors (Fig. 2b). Different from σ, S is negatively correlated with the carrier concentration,[7,33] hence the pure BiSbTe sample possessed larger S compared with the BiSbTe·x%CuO composites before intrinsic excitation (when the temperature was lower than 440 K). The maximum S (S_{max}) for the pure BiSbTe sample reaches 279 μV/K at 334 K, while S_{max} is lowered to 238 μV/K at 367 K for BiSbTe·0.05%CuO, and to 209 μV/K at 474 K for BiSbTe·0.1%CuO, respectively. For BiSbTe·0.2%CuO and BiSbTe·0.3%CuO composites, the temperature for S_{max} is beyond the measurement temperature (larger than 514 K). Therefore, S_{max} decreases with x, while the temperature for S_{max} increases with x. With the climbing of the measurement temperature, the S value of BiSbTe·x%CuO gradually exceeds that of the pure BiSbTe sample, yielding larger powder factors (PF) for BiSbTe·x%CuO composites (Fig. 2c). This probably leads to a pronounced zT at higher temperature after CuO doping. Additionally, the PF of BiSbTe·x%CuO composites are larger than the pure BiSbTe sample, in which the PF for the BiSbTe·0.3%CuO and pure BiSbTe composites are 2.26 and 0.72 mW/(m·K^2) at 514 K respectively.

As revealed above, due to the effective doping, small concentrations of CuO enhance the electrical conductivity of p-type BiSbTe nanocomposites significantly. Hall-effect measurements were performed to study the doping effect of CuO, from which the Hall carrier concentration n_H and mobility μ_H were extracted (Fig. S6). As the bipolar conduction is not significant at low temperature (e. g. 313 K), the n_H for all the BiSbTe·x%CuO composites (including pure BiSbTe samples) is mostly contributed by the majority carriers, i. e. holes. Due to the effective doping by CuO, n_H increases from 9.17×10^{18} cm^{-3} for the pure BiSbTe sample to 5.77×10^{19} cm^{-3} for BiSbTe·0.3%CuO sample. Also, the resulting mobility of the majority carriers (holes) as a function of temperature is obtained from the transport modeling, as is shown in Fig. S6b. The mobility steadily decreases with increasing CuO concentration due to the increased impurity scattering.

Annular dark-field imaging (HAADF) scanning transmission electron microscope (STEM) and energy dispersive spectroscopy (EDS) elemental mapping were utilized to study the solubility of CuO inside the

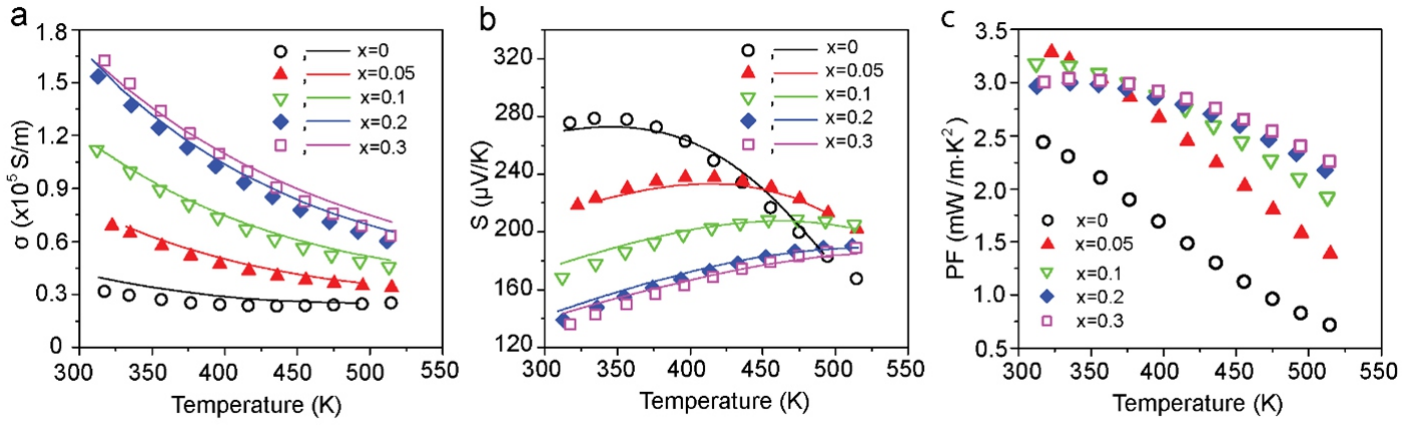

Fig. 2 Thermoelectric performance of BiSbTe·x%CuO. Electrical conductivity (σ, a), Seebeck coefficient (S, b) and power factor (PF, c) of BiSbTe·x%CuO with different CuO concentration x. Symbols are experimental data and the continuous curves are theoretical fittings based on the carrier transport modeling in (a) and (b).

BiSbTe matrix. The diameter of commercial CuO nanoparticles is 20~50 nm (Sigma-Aldrich), verified by the TEM image (Fig. S4). From the HAADF-STEM image and EDS mapping for the BiSbTe·0.3%CuO sample (Fig. 3), the Cu enrichment area has a size of ~47 nm, which matches the diameter of CuO nanoparticle very well. This also implies that Cu is not completely doped into BiSbTe. However, no oxygen enrichment is observed, suggesting that the oxygen is uniformly distributed inside the BiSbTe matrix.

The thermal conductivity κ_{tot} was measured by the laser-flash method. As was indicated from the temperature-dependent κ_{tot} in Fig. 4a, κ_{tot} ranges from 0.8 to 1.4 W/(m·K). With an increase of the concentration of CuO, κ_{tot} increases from 0.84 to 1.33 W/(m·K) at about 313 K, which is mainly contributed by the increase of the electronic thermal conductivity κ_e. The determination of κ_e is based on the Wiedemann-Franz law $\kappa_e=L\sigma T$, where L represents the Lorenz number. The calculation of L was performed using BTE modeling, as described in the Supplemental Information, and the temperature-dependent of L is shown in Fig. S5. As shown in Fig. 4b, κ_e increases with the CuO amount across the entire measurement temperature range, which is consistent with the trend of σ with CuO amount (Fig. 2a). As the CuO can significantly enhance σ, κ_e for BiSbTe·0.3%CuO is as large as 0.69 W/(m·K) at 313 K, while that of pure BiSbTe is only 0.15 W/(m·K). κ_{tot} can be expressed as $\kappa_e+\kappa_{bi}+\kappa_{lat}$. Based on our XRD spectra, SEM and TEM images (Fig. 1c, Fig. S3 and Fig. S4), the average grain size of BiSbTe is approximately 1 μm. By considering the grain size (related to the grain boundaries) and other defects in our BiSbTe·x%CuO composites including the antisite and interstitial defects, the simulation of κ_{lat} was performed via the phonon Boltzmann transport equation including all the phonon branches with the full dispersions shown in Fig. S7 obtained from first-principles DFT calculations. Compared with BiSbTe alloys, the 1 μm grain size leads to a reduced κ_{lat} from 0.82 W/(m·K) to 0.67 W/(m·K) for our pure BiSbTe composite (Fig. S8). With increasing CuO concentration, κ_{lat} is slightly reduced due to the increased phonon scattering induced by Cu and O (Fig. S9). However, the impact of CuO in the reduction of κ_{lat} is not significant due to the low concentration of CuO (the maximum concentration herein as only 0.3 %). The simulation shows that κ_{lat} can be further reduced by increasing the CuO concentration. The simulated κ_{lat} at 300 K is 0.67 W/(m·K) for pure BiSbTe sample and decreases to 0.62 W/(m·K) for the BiSbTe·0.3%CuO sample, as presented in Fig. 4c and Fig. S9. In addition, by subtracting κ_e from κ_{tot}, we obtained the temperature-dependent of $\kappa_{tot}-\kappa_e$ (Fig. 4c). It is notable that the calculated κ_{lat} agrees well with $\kappa_{tot}-\kappa_e$ initially at 313 K. With the increase of temperature, $\kappa_{tot}-\kappa_e$ gradually surpasses κ_{lat}. The discrepancy between them comes from the bipolar contribution, which becomes important when the concentration of minority carriers (electrons) increases, thus increasing the κ_{tot}. Compared with the slight difference in κ_{bi}, the $\kappa_{tot}-\kappa_e$ (i.e. $\kappa_{bi}+\kappa_{lat}$) shows a decreasing tendency with increasing CuO concentration. This result demonstrates that Cu and O doping can efficiently suppress the bipolar contribution. The κ_{bi} for the pure BiSbTe sample increases continuously with temperature from 0.04 W/(m·K) at 313 K to about 0.70 W/(m·K) at 492 K, while κ_{bi} for the BiSbTe·0.3%CuO sample is

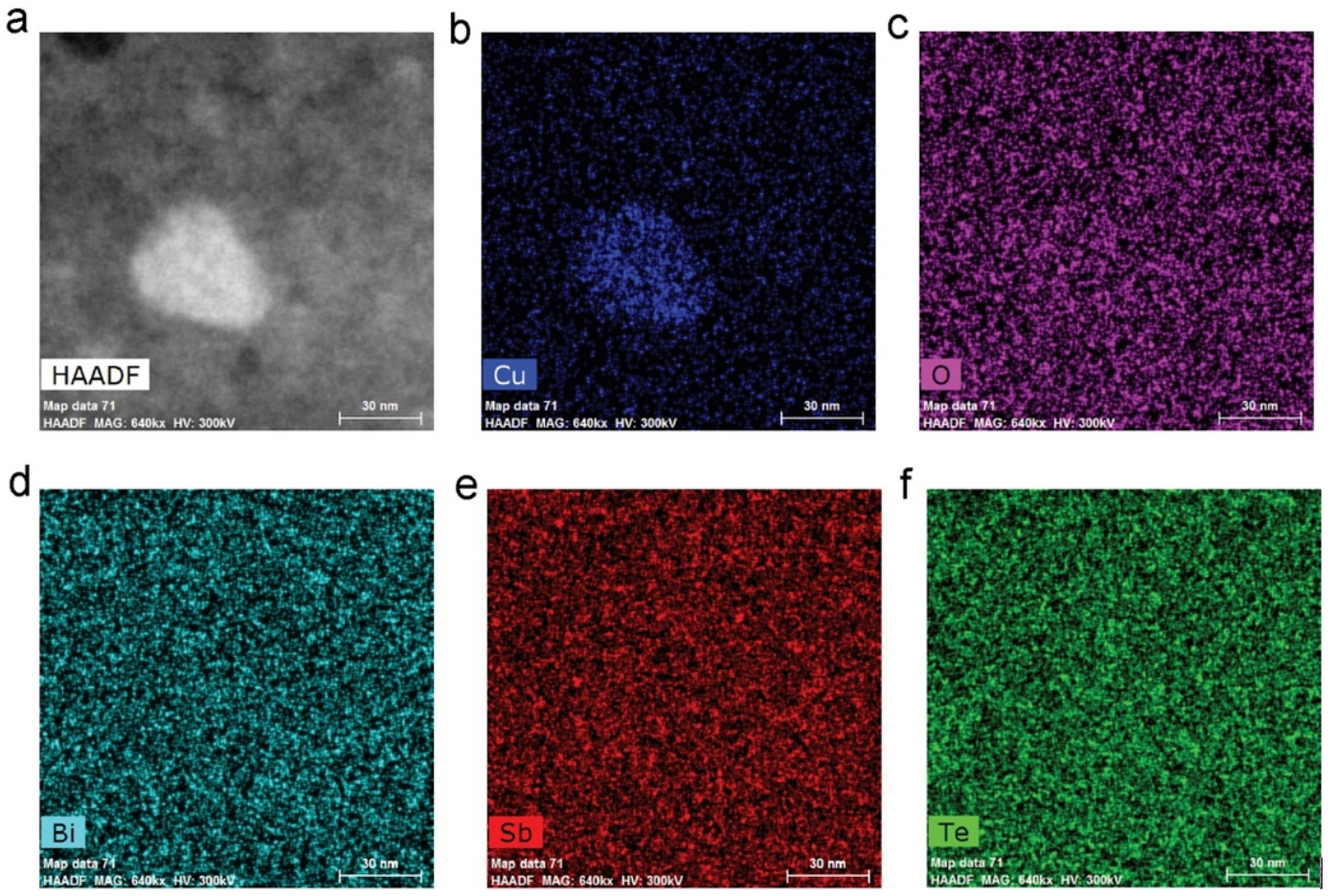

Fig. 3 HAADF-STEM image (a) and (b-f) EDS elemental mapping of the BiSbTe·0.3%CuO sample.

controlled within 0.08 W/(m·K) over a wide measurement temperature range (312~493 K). Therefore, there is a compromise between κ_e, κ_{lat} and κ_{bi}, where the increase of CuO concentration increases κ_e while lowering κ_{lat} and κ_{bi} simultaneously.

To explore the role of Cu and O doping using quantum mechanics, we have performed several DFT calculations, including spin-orbit coupling, which is necessary to reproduce the small energy gap that is measured experimentally. We found that Sb_2Te_3 and Bi_2Te_3 have very similar results and we therefore only discuss the results for the former. The possible doping defects from Cu and O are the substitution of Sb/Te atoms and the interstitial defects, respectively. The unit cell Energies of different compounds are listed in Table S2. The formation energies for all the defects are listed in Table 1. The calculation details are shown in Supplemental Information Section 4. The formation energy of different defects as a function of Cu chemical potential are plotted in Fig. S10. It is seen that the lowest-energy defects formed by Cu and O are the Cu substitution of Sb and the O interstitial defects, respectively.

Since it has been experimentally observed that Cu and O are separated after SPS and the hole concentration increases after CuO doping, we use DFT calculations to find out if these two kinds of defects can provide holes. We have calculated the projected densities of states (pDOS) for perfect Sb_2Te_3, Sb_2Te_3 with Cu_{Sb} defect, and Sb_2Te_3 with O interstitial defects as shown in Figs. 5a-c, respectively. The zero of energy is set at the top of the valence bands. It is clear that Cu doping introduces a substantial concentration of holes and the material remains semiconducting. The origin of p-type doping by substitutional Cu can be traced to the fact that, as shown in Fig. 5b, its ten 3*d* electrons lie deep inside the valence bands and its single 3*s* level spans the valence bands. Since Cu has an odd number of electrons and substitutes an atom with an even number of electrons, inevitably we end up with a hole concentration. Calculations of interstitial oxygen impurities again reveal that they dope the material p-type. As Fig. 5c shows, the 2*p* states of interstitial O lie deep in the valence bands. Since an O atom has only four 2*p* electrons and its 2*p* state, being within the valence bands, must be fully occupied with six electrons, it is inevitable that every interstitial O atom introduces two holes at the top of the valence bands. These results explain the observed enhanced p-type

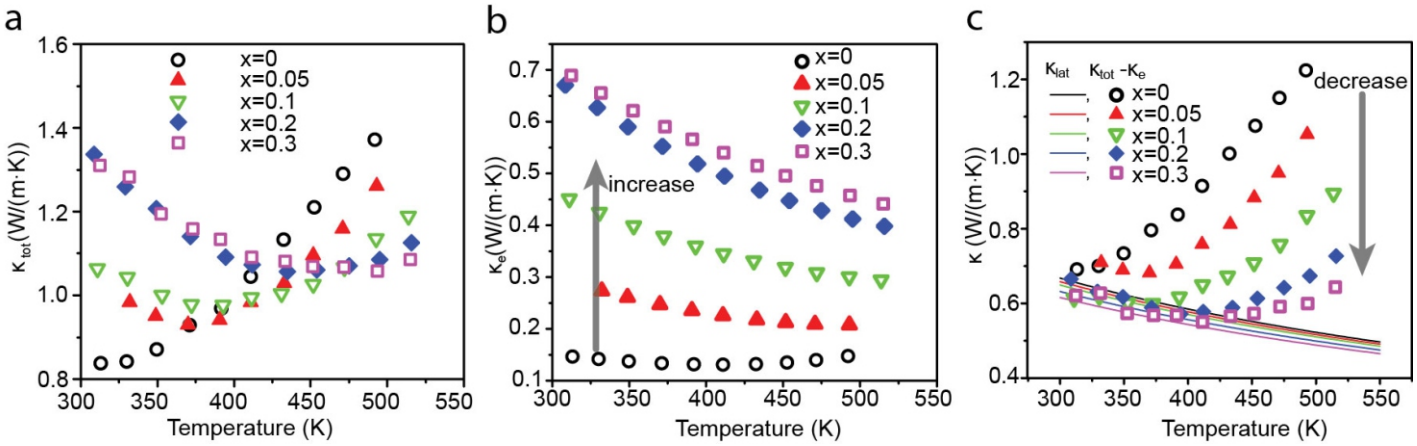

Fig. 4 Thermal conductivity of BiSbTe·x%CuO composites. (a) Total thermal conductivity κ_{tot} and (b) electronic thermal conductivity κ_e of BiSbTe·x%CuO composites; (c) Comparison of κ_{lat} and $\kappa_{tot} - \kappa_e$. The difference between them is the bipolar thermal conductivity contribution, which decreases with increasing CuO concentration as indicated by the thick downward grey arrow.

Table 1. The possible doping defects formed by Cu and O and their formation energies.

Possible doping mechanisms	Cu		O	
	Formation Energy	Provide holes?	Formation Energy	Provide holes?
Substitute Sb	**0.33 eV/atom**	**Yes**	2.37 eV/atom	Yes
Substitute Te	1.85 eV/atom	No	-0.50 eV/atom	No
Interstitial	0.85 eV/atom	No	**-1.40 eV/atom**	**Yes**

doping.

Benefiting from the effective p-doping from Cu and O, the figure of merit *zT* of BiSbTe·x%CuO nanocomposites is comprehensively improved, as presented in Fig. 5d. For pure BiSbTe, the *zT* over the entire measured temperature range is kept below 1.0 and decreases with measurement temperature. For BiSbTe·x%CuO with 0.05 %~0.3 % CuO concentration, the *zT* peak can reach 1.1~1.2, and the temperature for *zT* peak shows a dependence on the CuO concentration (Fig. S11). The temperature for *zT* peak was shifted from 317 K for pure BiSbTe to 377 K for BiSbTe·0.05%CuO, 395 K for BiSbTe·0.1%CuO, 452 K for BiSbTe·0.2%CuO and 475 K for BiSbTe·0.3%CuO. In addition, the *zT* can maintain a value above 1.0 over a wide temperature range. For example, *zT* of BiSbTe·0.1%CuO is over 1.0 from 330 to 474 K, which makes BiSbTe·x%CuO a very competitive thermoelectric material in solid-state cooling as well as waste heat recovery.

Additionally, owing to the superionic behavior in Cu-containing thermoelectric materials under an electrical load, the stability of Cu-containing thermoelectric materials remains a great concern.[34,35] Our BiSbTe·x%CuO composites show extremely good stability not only at inert atmosphere but also exposed to air. As shown in Fig. S12, the black plots correspond to the pristine electrical conductivity σ and Seebeck coefficient *S* of one BiSbTe·0.1%CuO sample. After the measurement, this sample was annealed at 475 K under argon atmosphere for 24 h, followed by the 2nd measurement of σ and *S* (red plots in Fig. 5b). It is found that both of σ and *S* do not change much. Furthermore, this sample was annealed for another 24 h at 475 K in air. The measurement results (green plots in Fig. S12) afterwards indicate that the sample is still stable and shows negligible change compared with its pristine state.

In summary, we for the first time realized effective doping of BiSbTe nanocomposites by metal oxide. Due to the remarkable increase of hole concentration and significant suppression of the bipolar effect, the thermoelectric properties, especially the electrical conductivity and bipolar thermal conductivity, have been controllably modulated by a small concentration of CuO doping (0.05 %~0.3 %). Consequently, the figure of merit has been comprehensively optimized, capable of reaching above 1.0 over a wide temperature range. In addition, CuO doping exhibits excellent stability. This new approach opens up new opportunities and insights for improving and effectively controlling the thermoelectric performance by chemical doping.

Acknowledgment

Y. W. thanks the support from Herbert L. Stiles Professorship. Theoretical work by T.L.F. and S.T.P. was supported in part by Department of Energy grant DE-FG0209ER46554 and by the McMinn Endowment. Computations at Vanderbilt University and ORNL were performed at the National Energy Research Scientific Computing Center (NERSC), a Department of Energy, Office of Science, User Facility funded through Contract No. DE-AC02-05CH11231. Computations also used the Extreme Science and Engineering Discovery Environment (XSEDE).

Supporting Information

Supporting Information includes the experimental, characterization and theoretical modeling parts, 12 Figures and 2 tables.

References

1. X. Shi, L. Chen and C. Uher, *Int. Mater. Rev.,* 2016, **61**, 379-415.
2. T. Zhu, L. Hu, X. Zhao and J. He, *Adv. Sci.,* 2016, **3**, 160004.
3. H. J. Goldsmid, *Materials,* 2014, **7**, 2577-2592.
4. J. P. Heremans, B. Wiendlocha and A. M. Chamoire, *Energy Environ. Sci.,* 2012, **5**, 5510-5530.
5. J. Li, Q. Tan, J. F. Li, D. W. Liu, F. Li, Z. Y. Li, M. Zou and K. Wang, *Adv.*

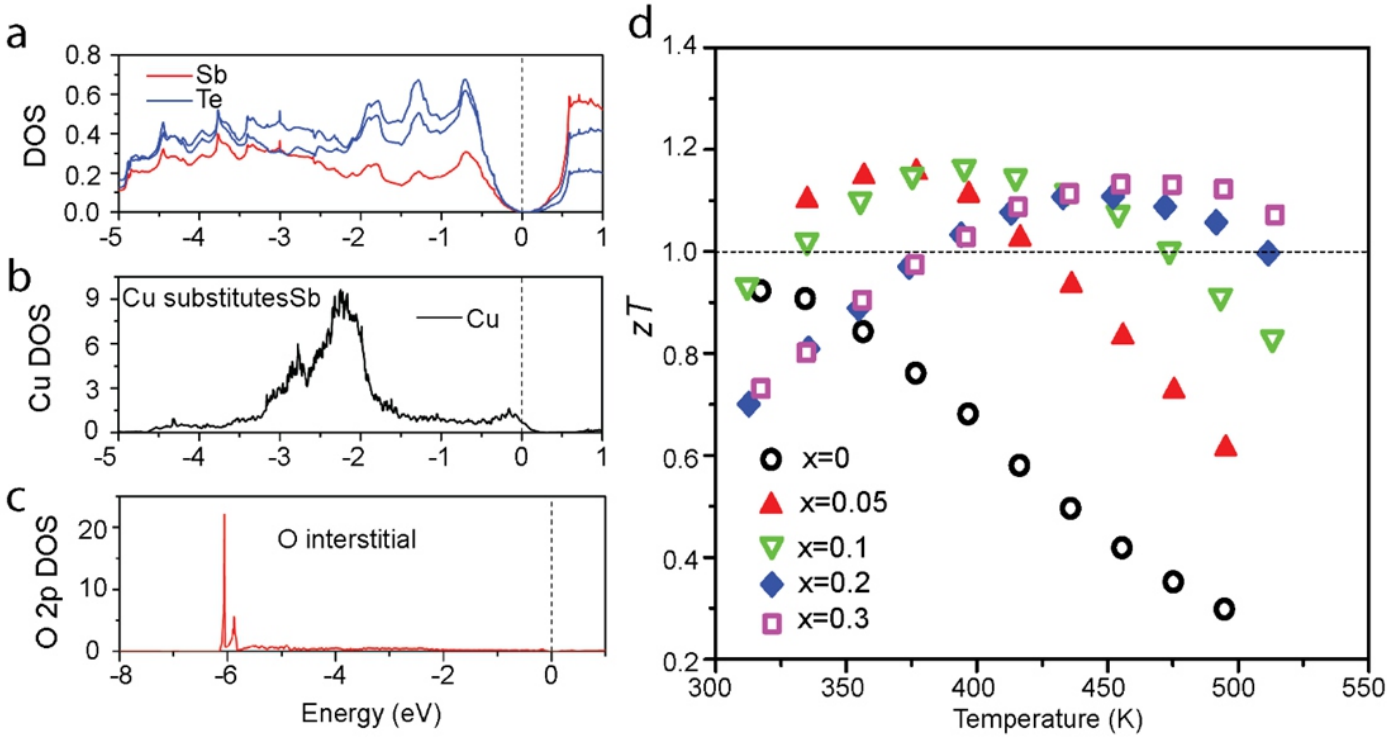

Fig. 5 DFT calculation and the figure of merit *zT*. Projected DOS for a perfect Sb_2Te_3 crystal; (a) and for an Sb_2Te_3 crystal doped with Cu substituting Sb (b); (c) The partial DOS of the 2p orbital of O as an interstitial defect in Sb_2Te_3 crystal; (d) Figure of merit *zT* of BiSbTe·x%CuO nanocomposites.

Func. Mater., 2013, **23**, 4317-4323.
6. S. I. Kim, K. H. Lee, H. A. Mun, H. S. Kim, S. W. Hwang, J. W. Roh, D. J. Yang, W. H. Shin, X. S. Li and Y. H. Lee, *Science,* 2015, **348**, 109-114.
7. T. Zhu, Y. Liu, C. Fu, J. P. Heremans, J. G. Snyder and X. Zhao, *Adv. Mater.,* 2017, **14**, 1605884.
8. L. Yang, Z. G. Chen, M. S. Dargusch and J. Zou, *Adv. Energy Mater*., 2017, **8**, 1701797.
9. B. Xu, T. Feng, Z. Li, W. Zheng and Y. Wu, *Adv. Mater.* 2018, e1801904.
10. Z. Chen, X. Zhang and Y. Pei, *Adv. Mater.* 2018, **30**, e1705617.
11. S. Lin, W. Li, S. Li, X. Zhang, Z. Chen, Y. Xu, Y. Chen and Y. Pei, *Joule,* 2017, **1**, 816–830.
12. Z. Chen, B. Ge, W. Li, S. Lin, J. Shen, Y. Chang, R. Hanus, G. J. Snyder and Y. Pei, *Nat. Commun.,* 2017, **8**, 13828.
13. F. Hao, P. Qiu, Q. Song, H. Chen, P. Lu, D. Ren, X. Shi and L. Chen, *Materials,* 2017, **10**, 251.
14. Y. Pan, U. Aydemir, F. H. Sun, C. F. Wu, T. C. Chasapis, G. J. Snyder and J. F. Li, *Adv. Sci.,* 2017, **4**, 1700259.
15. B. Xu, M. T. Agne, T. Feng, T. C. Chasapis, X. Ruan, Y. Zhou, H. Zheng, J. H. Bahk, M. G. Kanatzidis, G. J. Snyder and Y. Wu, *Adv. Mater.,* 2017, **29**, 1605140.
16. J. Horák, L. Tichy, P. Lostak and A. Vasko, *Cryst. Lattice Defects,* 1976, **6**, 233-238.
17. Q. Zhang, X. Ai, L. Wang, Y. Chang, W. Luo, W. Jiang and L. Chen, *Adv. Func. Mater.,* 2015, **25**, 966-976.
18. A. Banik, B. Vishal, S. Perumal, R. Datta and K. Biswas, *Energy Environ. Sci.,* 2016, **9**, 2011-2019.
19. C. Ou, J. Hou, T. R. Wei, B. Jiang, S. Jiao, J. F. Li and H. Zhu, *NPG Asia Mater.,* 2015, **7**, e182.
20. S. Ortega, M. Ibáñez, Y. Liu, Y. Zhang, M. V. Kovalenko, D. Cadavid and A. Cabot, *Chem. Soc. Rev.,* 2017, **46**, 3510-3528.
21. H. Ohta, K. Sugiura and K. Koumoto, *Inorg. Chem.,* 2008, **47**, 8429-8436.
22. K. Koumoto, Y. Wang, R. Zhang, A. Kosuga and R. Funahashi, *Annu. Rev. Mater. Res.,* 2010, **40**, 363-394.
23. T. Zhang, Q. Zhang, J. Jiang, Z. Xiong, J. Chen, Y. Zhang, W. Li and G. Xu, *Appl. Phys. Lett.* 2011, **98**, 022104.
24. Y. Li, G. Liu, X. Qin and F. Shan, *RSC Adv.,* 2016, **6**, 112050-112056.
25. B. Madavali, H. S. Kim, K. H. Lee and S. J. Hong, *J. Appl. Phys.,* 2017, **121**, 225104.
26. J. Bludská, I. Jakubec, Č. Drašar, P. Lošťák and J. Horák, *J. Philos. Mag.,* 2007, **87**, 325-335.
27. H. J. Yu, M. Jeong, Y. S. Lim, W. S. Seo, O. J. Kwon, C. H. Park and H. J. Hwang, *RSC Adv.,* 2014, **4**, 43811-43814.
28. H. J. Wu and W. T. Yen, *Acta Mater.,* 2018, **157**, 33–41.
29. K. Biswas, J. He, I. D. Blum, C. I. Wu, T. P. Hogan, D. N. Seidman, V. P. Dravid and M. G. Kanatzidis, *Nature,* 2012, **489**, 414-418.
30. G. Han, Z. G. Chen, L. Yang, M. Hong, J. Drennan and J. Zou, *ACS Appl. Mater. Interfaces,* 2014, **7**, 989-995.
31. Y. Zheng, Q. Zhang, X. Su, H. Xie, S. Shu, T. Chen, G. Tan, Y. Yan, X. Tang, C. Uher and G. J. Snyder, *Adv. Energy Mater.,* 2015, **5**, 1401391.
32. J. H. Bahk and A. Shakouri, A. *Phys. Rev. B,* 2016, **93**, 165209.
33. G. J. Snyder and E. S. Toberer, *Nat. Mater.,* 2008, **7**, 105-114.
34. G. Dennler, R. Chmielowski, S. Jacob, F. Capet, P. Roussel, S. Zastrow, K. Nielsch, I. Opahle and G. K. H. Madsen, *Adv. Energy Mater*., 2014, **4**, 1301581.
35. H. Liu, X. Shi, F. Xu, L. Zhang, W. Zhang, L. Chen, Q. Li, C. Uher, T. Day and G. J. Snyder, *Nat. Mater.,* 2012, **11**, 422-425.

Electronic Supplementary Information

Experimental and Theoretical Study on Well-Tunable Metal Oxide Doping Towards High-Performance Thermoelectrics

Enzheng Shi[#], Tianli Feng[#], Je-Hyeong Bahk, Yu Pan, Wei Zheng, Zhe Li, G. Jeffery Snyder, Sokrates T. Pantelides, Yue Wu[*]

Part 1. Spark plasma sintering, characterization and measurement

This mixture powder was loaded into a graphite die (Φ=10.2 mm) and sealed by two graphite punches (Φ=10 mm). Afterwards, the packed die and punches were transferred into a Fuji-211lx spark plasma sintering (SPS) system. The SPS condition is set as follows: axial pressure of 50 MPa, sintering at 480^{o}C for 5 min. After the sintering, the graphite die should be cooled down at a rate of 10^{o}C/min.

The morphology, micro-structure of BiSbTe·x%CuO samples were characterized by SEM (FEI Quanta 250 FE-SEM) and TEM (FEI Tecnai G2-F20, 200 kV). The HAADF-STEM and EDS elemental mapping of the BiSbTe·0.3%CuO sample were performed a FEI Titan Themis Cs-corrected TEM at 300 kV. Samples for TEM and EDS elemental mapping were prepared using a focused ion beam (FIB, Helios Dual Beam, FEI).

Electrical conductivity and Seebeck coefficient were measured on Linseis LSR-3 system by a four-probe configuration. The total thermal conductivity (κ_{tot}) is expressed as $\kappa_{tot} = D_T \cdot C_p \cdot \rho$, where D_T is the thermal diffusivity, ρ is the mass density and C_p is the heat capacity. D_T is measured using laser flash method in a Linseis XFA 600. The Dulong-Petit C_p was used herein.

Part 2. Measurement of Hall coefficient

Hall coefficients (R_H) were measured using van der Pauw method under a 2 T magnetic field.[1] Measurements were conducted under vacuum with a heating rate of 1.5 K/min. Hall carrier concentration (n_H) and mobility (μ_H) were calculated by $n_H=1/(eR_H)$ and $\mu_H=R_H/\rho$, where ρ is electrical resistivity.

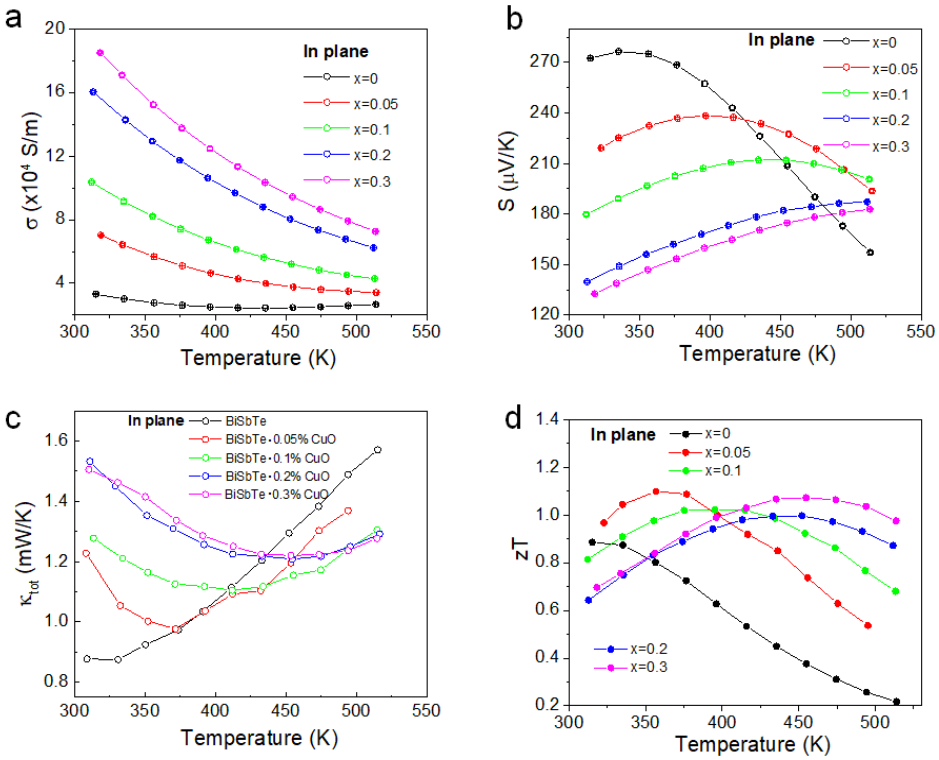

Figure S1. Thermoelectric properties of the BiSbTe·x%CuO composites (x=0-0.3), including the electrical conductivity (a), Seebeck coefficient (b), thermal conductivity (c) and figure of merit (d). Compared with those along cross-plane direction, it is noted that the figure of merit along cross plane is larger.

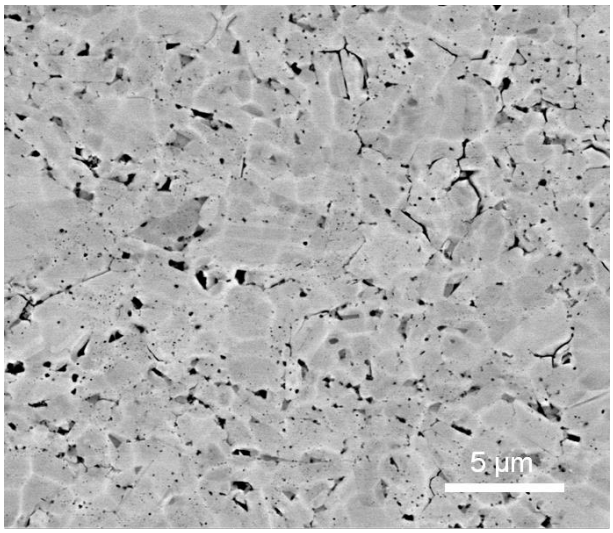

Figure S2. Back-scattering SEM image of pure BiSbTe sample.

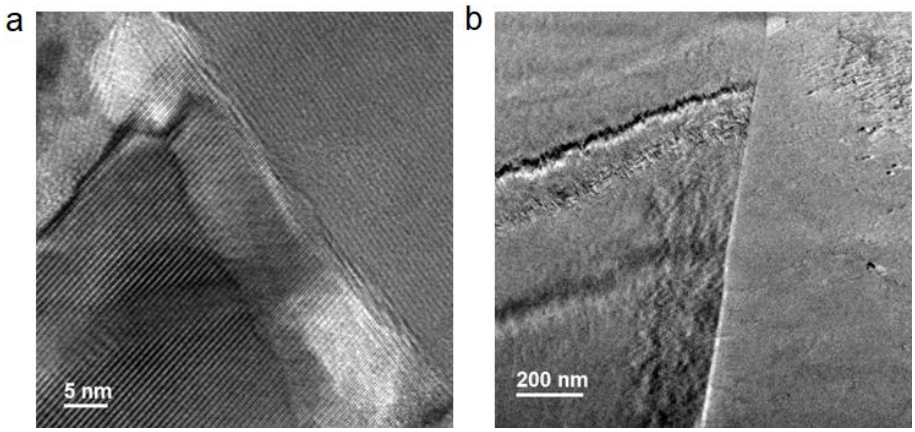

Figure S3. TEM images of BiSbTe·0.1%CuO nanocomposites.

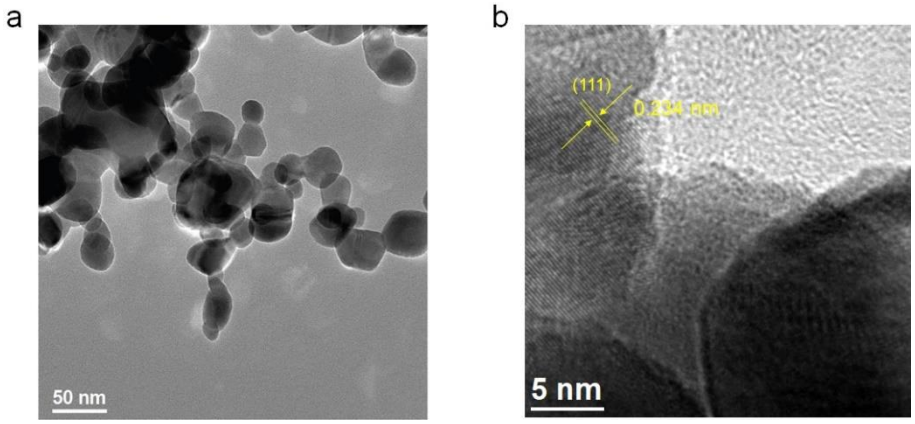

Figure S4. TEM images of CuO nanoparticles. The crystal plane (111) can be identified from the high-resolution TEM image (b).

Part 3. Theoretical Modeling

3.1 Carrier transport modeling

We performed the carrier transport modeling based on the linearized Boltzmann transport equations (BTE) under the relaxation time approximation for the curve fitting of the experimental electrical conductivity and Seebeck coefficient, and the calculations of the Lorenz number for thermal conductivity analysis. More information about the modeling can be found in Ref. [2].

In the modeling, all of the carrier transport properties are expressed as integral functions of the differential conductivity $\sigma_d(E)$ over carrier energy E, defined as

$$\sigma_d(E) = e^2\tau(E)v^2(E)\rho_{DOS}(E)\left(-\frac{\partial f_0}{\partial E}\right), \quad \text{(S1)}$$

where e is the electron charge, τ is the relaxation time, ρ_{DOS} is the density of states, v is the carrier velocity and f_0 is the Fermi-Dirac distribution. For the multiple-band transports in BiSbTe, the transport properties are calculated in each of the bands with the relative position of the Fermi level E_F from the band extremum and the contributions from each band are then added together to find the total transport values in the bulk. The electrical conductivity σ, the Seebeck coefficient S, and the electronic thermal conductivity are given, respectively, by

$$\sigma = \sum_i \int \sigma_{d,i}(E)dE, \quad \text{(S2)}$$

$$S = \sum_i \frac{1}{qT}\frac{\int \sigma_{d,i}(E)(E - E_{F,i})dE}{\sigma}, \quad \text{(S3)}$$

$$\kappa_{\text{elect}} = \sum_i \frac{1}{q^2T}\int (E - E_{F,i})^2 \sigma_{d,i}(E)dE - S^2\sigma T, \quad \text{(S4)}$$

where Σ is the sum over the bands, q is $-e$ for the conduction bands and $+e$ for the valence bands, T is the absolute temperature, and E_F is the Fermi energy. Carrier mobility of each type is found from $\mu_h = \sigma_h/pe$ for holes with p being the hole concentration, and $\mu_e = \sigma_e/ne$ for electrons with n being the electron concentration.

The Lorenz number is given by

$$L = \sum_i \frac{1}{q^2T^2}\frac{\int \sigma_{d,i}(E)(E - E_{F,i})^2 dE}{\sigma} - S^2. \quad \text{(S5)}$$

This Lorenz number is a function of band structure and the Fermi level (or carrier concentration). Figure S5 below shows the Lorenz number as a function of temperature for the BiSbTe·x%CuO samples. The Lorenz numbers are found to be much smaller than the conventional value (2.44×10^{-8} W Ω K^{-2}), which is valid only for metals and very highly-

doped semiconductors. The Lorenz numbers are also lower than the typical values (1.5 ~ 2.44 × 10^{-8} W Ω K^{-2}) found for the state-of-the-art thermoelectric materials because of the multiple bands and low carrier concentrations (and consequently low Fermi levels).[3]

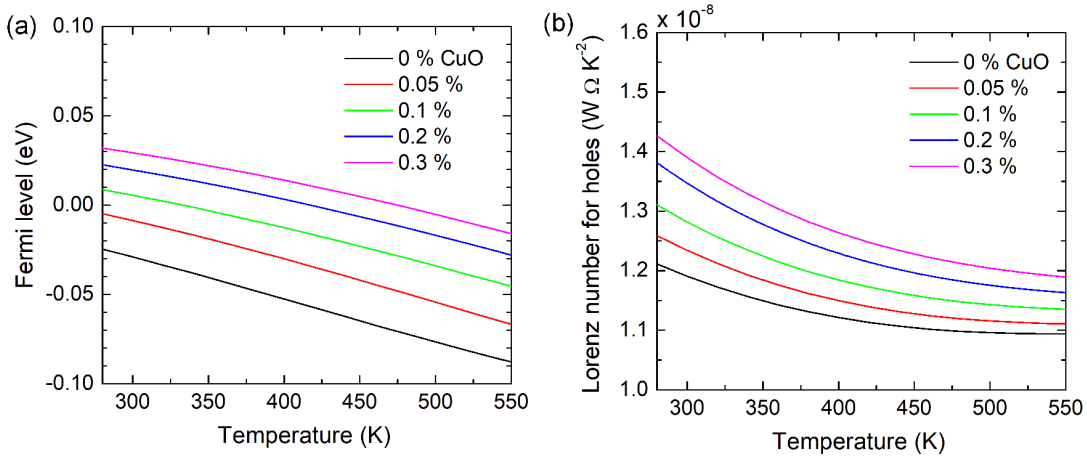

Figure S5. (a) Fermi level in reference to the valence band maximum, and (b) Lorenz number as a function of temperature for the CuO-doped BiSbTe samples calculated from the carrier transport modeling.

The total electrical conductivity and the total Seebeck coefficient in the two-type carrier transport are obtained by

$$\sigma = \sigma_e + \sigma_h, \tag{S6}$$

$$S = \frac{\sigma_e S_e + \sigma_h S_h}{\sigma_e + \sigma_h}, \tag{S7}$$

Since the partial Seebeck coefficients of electrons and holes possess the opposite signs, the magnitude of total Seebeck coefficient *S* is reduced by the bipolar transport. The total electronic thermal conductivity is not only the sum of the partial electronic thermal conductivities of electrons and holes. Another term from the bipolar thermodiffusion effect must be added to the total electronic thermal conductivity. The bipolar electronic thermal conductivity is given by

$$\kappa_{bi} = \frac{\sigma_e \sigma_h}{\sigma_e + \sigma_h}\left(S_e - S_h\right)^2 T. \tag{S8}$$

The relevant carrier scattering parameters from the acoustic phonon deformation scattering, short-range defect scattering, and ionized impurity scattering have been further adjusted to fit the electrical conductivity of the samples. No additional parameters have been adjusted for Seebeck coefficient fitting.

The Hall coefficient in the bipolar transport regime is a function of the carrier concentrations and mobilities of both carrier types following the equation as

$$R_H = \frac{1}{e}\frac{p - nb^2}{(p + nb)^2} \tag{S9}$$

Where p and n are the hole and electron concentration, respectively and b(= μ_e/μ_h) is the mobility ratio between electrons and holes. The band structure model and transport parameters enable estimating all the four properties of both carrier types, and thus estimating the Hall coefficient. Figure S6a shows the fitting results of the experimental Hall coefficients with the theory. Also shown in Figure S6b is the resulting mobility of the majority carrier (hole) as a function of temperature obtained from the transport modeling. Also, the mobility steadily decreases with increasing CuO content due to the increased impurity scatterings.

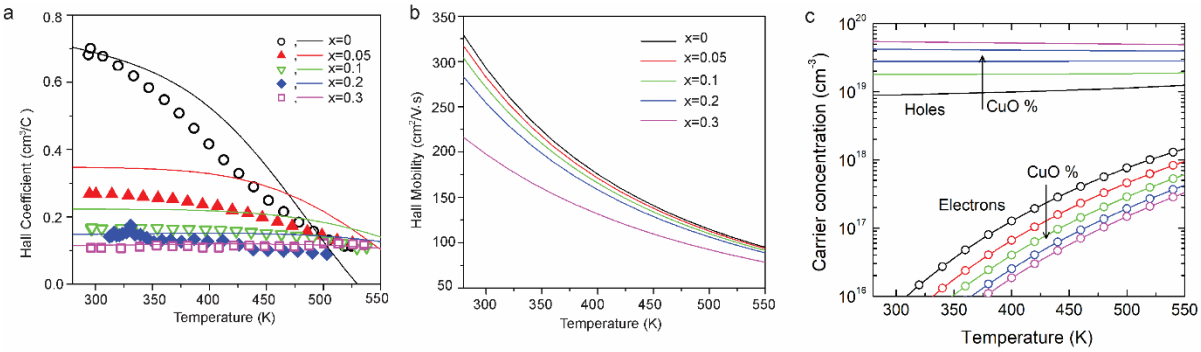

Figure S6. Hall-effect measurement and calculation of BiSbTe·x%CuO samples. (a). Hall coefficient, both experimental (symbols) and theoretical (curves) and (b) calculated hole (majority carrier) mobility as a function of temperature for the CuO-doped BiSbTe samples. (c) The dependence of electron and hole concentration with temperature for the CuO-doped BiSbTe samples.

3.2 Phonon Boltzmann transport equation model

The lattice thermal conductivity can be calculated by the Boltzmann transport equation[1],

$$\kappa_{lat} = \frac{4\pi}{3}\frac{1}{(2\pi)^3}\sum_{\nu}^{15}\int_{q}\frac{\hbar^2\omega^2(\mathbf{q},j)}{k_B T^2}\frac{e^{\frac{\hbar\omega(\mathbf{q},j)}{k_B T}}}{(e^{\frac{\hbar\omega(\mathbf{q},j)}{k_B T}}-1)^2}\upsilon_{ph}{}^2(\mathbf{q},j)\tau_{ph}(\mathbf{q},j)q^2 dq. \quad \text{(S10)}$$

$\hbar$ is Plank constant, k_B Boltzmann constant, T temperature, ω the phonon angular frequency, $\mathbf{q}$ the phonon wavevector, j phonon branch, υ_{ph} phonon group velocity, τ_{ph} phonon relaxation time, and q phonon wavevector magnitude. Since Bi_2Te_3 and Sb_2Te_3 are anisotropic, the thermal conductivity is averaged along three directions since the nano grain orientations in the nanocomposites are randomly distributed. In Eq. (S10), the summation over j is taken over all the phonon branches. Our model is more sophisticated than the commonly used Debye model, in which only the three acoustic phonon branches with linear dispersion relations are considered and thus the Debye model only works for the materials with no or a few optical branches.[4]

Bi_2Te_3 and Sb_2Te_3, however, have three "dispersive" acoustic branches and 12 optical branches. It has been shown that the four low-energy optical phonon branches have a large contribution (50%) to the total lattice thermal conductivity.[5] Thus, the Debye model is not suitable for Bi_2Te_3 and Sb_2Te_3. In the present work, we include the full phonon dispersion including three acoustic branches and all the 12 optical branches. The porosity is about P=2.5% and thus the lattice thermal conductivity reduction due to pores is about $(1\text{-}P)^{3/2}$=3.7%, which is quite small but included in the final results.

To obtain the lattice thermal conductivity by Eq. (S10), we have conducted first principles calculations using density functional theory (DFT) to calculate the phonon dispersion relations of Bi_2Te_3 and Sb_2Te_3. DFT was implement via the VASP program package,[6, 7] employing the projector augmented wave method (PAW) under local density approximation. The computational details are the same for Bi_2Te_3 and Sb_2Te_3. The structures were relaxed via the primitive unit cell with a convergence of 10^{-7} eV for the total energy, and 10^{-5} eV/Å for the forces on each atom. The relaxed lattice constants for Bi_2Te3 and Sb_2Te_3 are a=4.3550 Å, c= 29.8887 Å and a= 4.2530 Å, c= 29.4679 Å, respectively, which agree well with the literature.[8, 9] The plane-wave energy cutoff is 500 eV. The electronic k-space integration was performed with the tetrahedron method, involving a Γ-centered 12×12×12 k-mesh. The phonon dispersion is calculated via 2×2×2 primitive cells (40 atoms) by the density functional perturbation theory (DFPT) using the PHONOPY package with a Γ-centered 6 × 6 × 6 k-mesh.[10] Spin orbital coupling is not included as it is not critical for lattice vibration properties.[5, 8, 9]. The calculated phonon dispersion relations of Bi_2Te_3 and Sb_2Te_3 are shown in Figure S7, which agree well with literature.[5, 8, 9]

The phonon group velocity $v_{ph}(\mathbf{q}, j)$ was calculated from the dispersion by taking the differential $v_{ph} = d\omega/d\mathbf{q}$. The phonon relaxation time $\tau_{ph}(\mathbf{q}, j)$ is given by Matthiessen's rule,

$$\frac{1}{\tau_{ph}(\mathbf{q}, j)} = \frac{1}{\tau_{ah}(\mathbf{q}, j)} + \frac{1}{\tau_{mass}(\mathbf{q}, j)} + \frac{1}{\tau_{gb}(\mathbf{q}, j)} + \frac{1}{\tau_{np}(\mathbf{q}, j)} + \frac{1}{\tau_{Ox}(\mathbf{q}, j)}. \quad \text{(S11)}$$

The terms on the right-hand side are the scattering rates induced by the lattice anharmonicity, Bi-Sb alloy mass disorder, $Bi_{0.5}Sb_{1.5}Te_3$ grain boundaries, Cu nanoparticles and O point defects, respectively. They are calculated by

$$\frac{1}{\tau_{ah}(\mathbf{q}, j)} = \frac{Ak_BT}{M_a v^2(\mathbf{q}, j)} \frac{\gamma^2 \omega^2(\mathbf{q}, j)}{\omega_{\max}(j)} \exp\left(-\frac{\hbar \omega_{\max}(j)}{3k_BT}\right), \quad \text{(S12)}$$

$$\frac{1}{\tau_{mass}(\mathbf{q}, j)} = \frac{\pi}{2} g_{mass} \omega^2(\mathbf{q}, j) DOS(\omega), \quad \text{(S13)}$$

$$\frac{1}{\tau_{gb}(\mathbf{q}, j)} = \frac{v(\mathbf{q}, j)}{D_{BiSbTe}}, \tag{S14}$$

$$\frac{1}{\tau_{np}(\mathbf{q}, j)} = v(\mathbf{q}, j)\left(\sigma_s^{-1} + \sigma_l^{-1}\right)^{-1} n_{np}, \tag{S15}$$

$$\sigma_s = 2\pi R_{np}^2,\ \sigma_l = \frac{4}{9}\pi R_{np}^2 \left(\Delta\rho / \rho\right)^2 (\omega R_{np} / v)^4, \tag{S16}$$

$$\frac{1}{\tau_{Ox}(\mathbf{q}, j)} = \frac{\pi}{2} g_{Ox}\omega^2(\mathbf{q}, j)DOS(\omega), \tag{S17}$$

respectively.

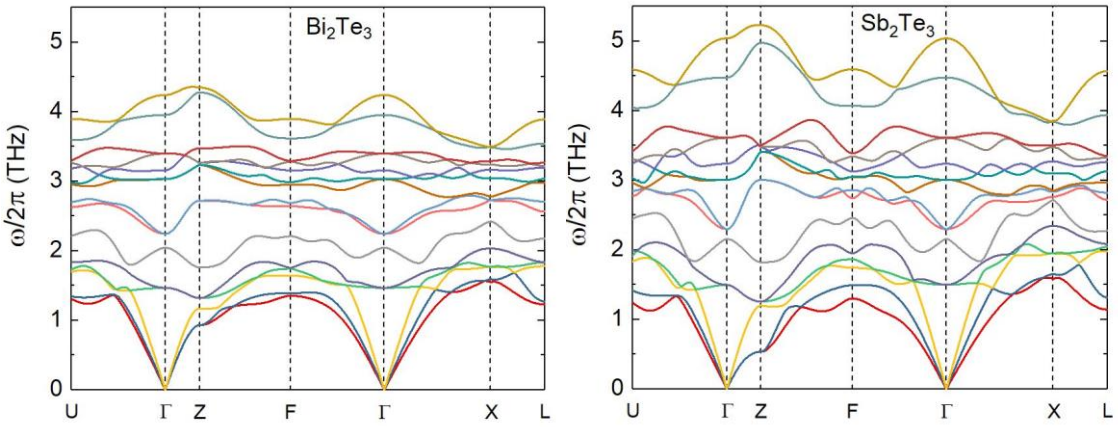

Figure S7. Phonon dispersion relations of Bi_2Te_3 and Sb_2Te_3 calculated from first principles based on density functional theory.

Equation (S12), anharmonic phonon scattering,[4] is determined by the two substance Bi_2Te_3 and Sb_2Te_3. $\omega_{max}(j)$ is the maximum frequency of the phonon branch j. γ is the Grüneisen parameter with the values 1.5 and 1.7 for Bi_2Te_3 and Sb_2Te_3, respectively.[11] M_a is the average atomic mass, given by

$$M_a = \frac{\alpha_{Bi}M_{Bi} + \alpha_{Sb}M_{Sb} + \alpha_{Te}M_{Te}}{\alpha_{Bi} + \alpha_{Sb} + \alpha_{Te}}, \tag{S18}$$

where α is the stoichiometric coefficient. The values of the coefficient A, 0.83 and 0.66 for Bi_2Te_3 and Sb_2Te_3 respectively, are pre-determined by pure Bi_2Te_3 and Sb_2Te_3, respectively.[12, 13]

The second term (Eq. (S13)) is induced by the Bi-Sb mass disorder.[14] In Eq. (S12), $DOS(\omega)$ is the normalized phonon density of states. g_{mass} represents the alloying mass disorder induced by the mass difference between Bi and Sb atoms, given by

$$g_{mass} = \frac{\alpha_{Bi}}{\alpha_{Bi} + \alpha_{Sb}}\left(1 - \frac{M_{Bi}}{\bar{M}_{BiSb}}\right)^2 + \frac{\alpha_{Sb}}{\alpha_{Bi} + \alpha_{Sb}}\left(1 - \frac{M_{Sb}}{\bar{M}_{BiSb}}\right)^2, \tag{S19}$$

$$\bar{M}_{BiSb} = \frac{\alpha_{Bi} M_{Bi} + \alpha_{Sb} M_{Sb}}{\alpha_{Bi} + \alpha_{Sb}}. \quad \text{(S20)}$$

This model has been shown to be accurate in capturing the alloy and impurity scattering for several systems.[4, 15-18]

The grain boundary scattering[4] in Eq. (S14) is determined by the grain diameter D_{BiSbTe}, which is a fitting parameter that is estimated as ~ 1 μm, a plausible value observed from experimental SEM and TEM images.

The Cu nanoparticle scattering (Eq. (S15)) interpolates between the short and long wavelength regimes.[19, 20] $\Delta\rho$ is the density difference between embedded nanoparticles and the bulk material; and ρ is the density of the bulk material. This model has been shown to give excellent estimation of nanoparticle scattering in several works.[20-22] The nanoparticle diameter is about 20-50 nm, and we take the average value 35 nm. Based on the Cu mass densities and particle sizes, the Cu nanoparticle concentration n_{np} for the 0.05%, 0.1%, 0.2% and 0.3% CuO samples are obtained as 2.4 $\times 10^{13}$, 4.8$\times 10^{13}$, 9.6$\times 10^{13}$ and 1.44$\times 10^{14}$ cm^{-3}, respectively.

The oxygen point defect scattering is shown in Eq. (S17).[15] g_{Ox} represents the mass disorder induced by oxygen atoms:

$$g_{Ox} = \frac{\alpha_{Ox}}{\alpha_{Ox} + \alpha_{BiSb}} \left(1 - \frac{M_{Ox}}{M_{BiSb}}\right)^2, \quad \text{(S21)}$$

where $M_{BiSb} = 0.25 M_{Bi} + 0.75 M_{Sb}$, the average mass of Bi and Sb. From Eq.(S10) to Eq.(S21), all the other parameters are pre-determined except the grain diameter D_{BiSbTe}, which is a fitting parameter. All the predetermined parameters' values are summarized in Table 1. The BiSbTe grain diameter D_{BiSbTe} is fitted as 1 μm, which agrees well with the experimental estimation.

Table. S1. Predetermined parameters used in the lattice thermal conductivity calculations.

Alloy mass disorder g_{mass}	0.0692
$Bi_{0.5}Sb_{1.5}Te_3$ density	6.8 g/cm^3
CuO density	6.32 g/cm^3
Pristine material anharmonic parameter A	0.83 for Bi_2Te_3, 0.66 for Sb_2Te_3
Gruneissen parameter γ	1.5 for Bi_2Te_3, 1.7 for Sb_2Te_3
Cu nanoparticle diameter $D_{np} = 2R_{np}$	35 nm
Cu nanoparticle concentration n_{np}	2.4, 4.8, 9.6 and14.4$\times 10^{13}$ cm^{-3} for 0.05%, 0.1% 0.2%, 0.3%-CuO

O point defect disorder factor g_{Ox}	0.0011, 0.0022, 0.0045, 0.00684 for 0.05%, 0.1% 0.2%, 0.3%-CuO

The effect of alloying and grain boundaries on suppressing the lattice thermal conductivity is shown in Figure S8. The mass disorder induced by alloying reduces the room-temperature thermal conductivity of Bi_2Te_3 (1.6 W/m-K) and Sb_2Te_3 (2.4 W/m-K) to 0.82 W/m-K. And, the BiSbTe grain with diameter $D = 1$ μm reduces κ_{lat} further to 0.67 W/m-K at room temperature. The effect of CuO insertion on the lattice thermal conductivity is shown in Figure S9. The decrease of κ_{lat} as a function of CuO concentration is clearly seen.

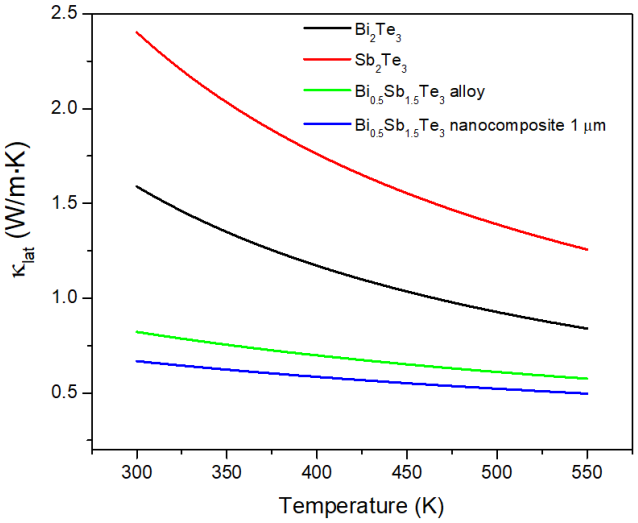

Figure S8. The calculated thermal conductivity for Bi_2Te_3, Sb_2Te_3, $Bi_{0.5}Sb_{1.5}Te_3$ alloy and $Bi_{0.5}Sb_{1.5}Te_3$ (grain size D = 1 μm) nanocomposite. The 1-μm gain size reduces the thermal conductivity of $Bi_{0.5}Sb_{1.5}Te_3$ alloy from 0.82 to 0.67 W/m·K for nanocomposites. The value 0.67 W/m·K agrees well with κ_{tot}-κ_e, the measured total thermal conductivity subtracted by the unipolar electronic contribution.

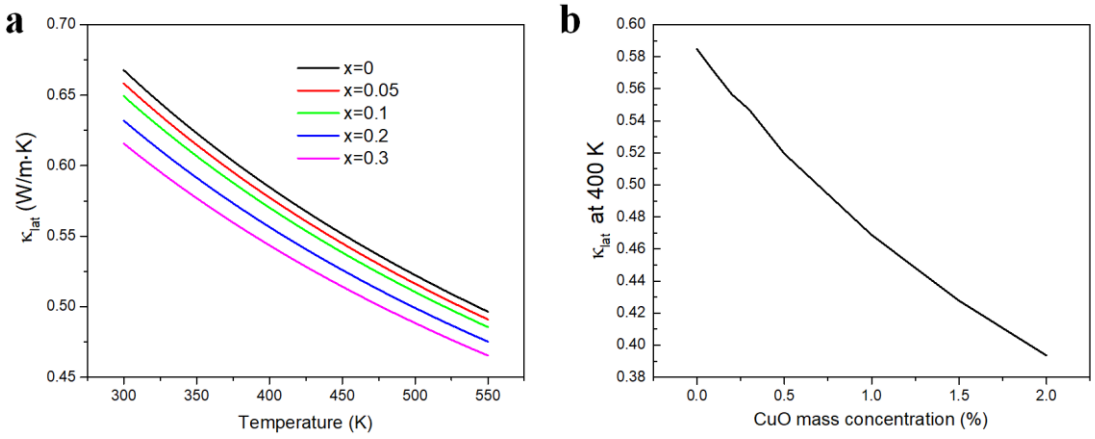

Figure S9. The effect of CuO insertion on the lattice thermal conductivity. (a) Enlarged plots

of temperature dependence of κ_{lat} for BiSbTe·x%CuO composites with different CuO concentration, corresponding to the plots in Figure 4c; (b). Calculated CuO concentration dependence of κ_{lat} of BiSbTe·x%CuO composites. It can be seen that the lattice thermal conductivity can be further reduced by increasing the CuO concentration.

Part 4. First-principles calculations of the electronic density of states of Sb_2Te_3 and Bi_2Te_3 with Cu and O dopings

To study the roles of Cu and O dopants in Sb_2Te_3 and Bi_2Te_3, we have performed first principles calculations using density functional theory (DFT) implemented in the VASP program package,[6, 7] employing the projector augmented wave method (PAW) under local density approximation. Spin-orbital coupling is included in all the calculations. The electronic properties of pristine Bi_2Te_3 and Sb_2Te_3 were calculated in a primitive cell (5 atoms). The atoms were relaxed with a convergence of 10^{-7} eV for the total energy, and 10^{-5} eV/Å for the forces on each atom. The plane-wave energy cutoff is 500 eV. The electronic k-space integration was performed with the tetrahedron method, involving a Γ-centered 12×12×12 k-mesh. The doped properties were calculated by using a 2×2×2 primitive cells (40 atoms). The atoms were relaxed with a convergence of 10^{-6} eV for the total energy, and 10^{-3} eV/Å for the forces on each atom. The electronic k-space integration was performed with the tetrahedron method, involving a Γ-centered 6×6×6 k-mesh. The formation energy of the substitutional defects are calcualted by ΔE = E(Sb_2Te_3 with Cu/O substitution of Sb/Te) + E(Sb/Te crystal) - E(Cu metal/ O_2 gas) - E(Sb_2Te_3). The energy for interstial defect is ΔE = E(Sb_2Te_3 with Cu/O interstitial) - E(Cu metal) - E(Sb_2Te_3).

Table S2. The energies (potentials) of the metals and compondes for the calculation of formation energies.

Defects	**eV**
Cu	-4.71510
Sb	-4.81443
Te	-3.80422
O_2 (gas)	-9.60814
CuO	-11.7276
Sb_2O_3	-33.8149

Sb_2Te_3	-21.6336
$Sb_{2x-1}CuTe_{3x}$(Cu substitutes Sb)	-583.2539 (x=27)
$Sb_{2x}CuTe_{3x-1}$(Cu substitutes Te)	-583.1663 (x=27)
$Sb_{2x}CuTe_{3x}$(Cu interstitial)	-587.9730 (x=27)
$Sb_{2x-1}OTe_{3x}$(O substitutes Sb)	-581.7235 (x=27)
$Sb_{2x}OTe_{3x-1}$(O substitutes Te)	-585.6124 (x=27)
$Sb_{2x}OTe_{3x}$(O interstitial)	-590.3154 (x=27)

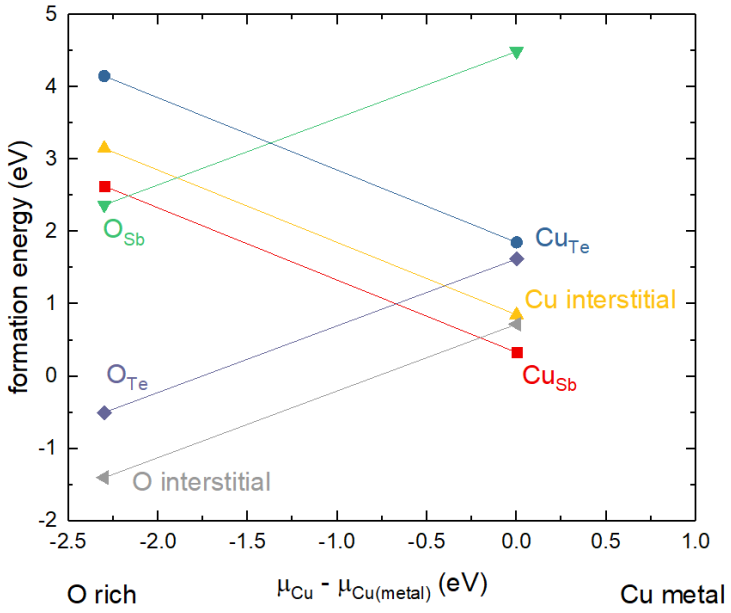

Figure S10. Formation energy of different defects as a function of Cu chemcial potential.

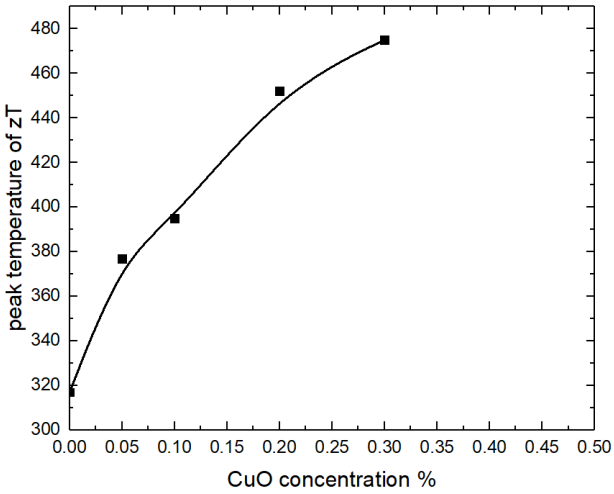

Figure S11. Peak temperature of *zT* as a function of CuO concentration.

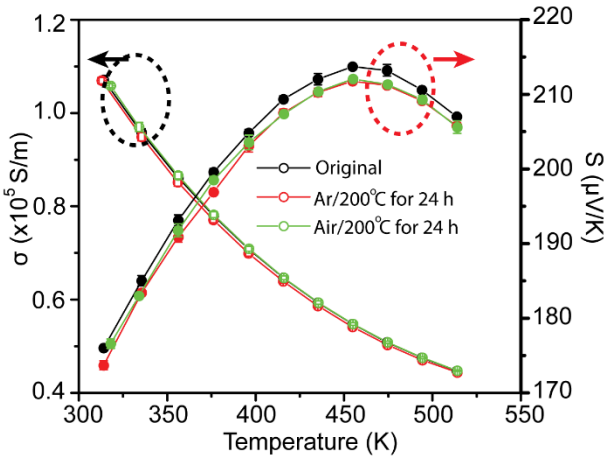

Figure S12. The comparison of electrical conductivity and Seebeck coefficient of BiSbTe·0.1%CuO after annealing under Ar/200 ºC for 24 h (red) and subsequent annealing under air/ 200ºC for 24 h (green).

References

1. K. A. Borup, E. S. Toberer, L. D. Zoltan, G. Nakatsukasa, M. Errico, J.-P. Fleurial, B. B. Iversen, G. J. Snyder, *Review of Scientific instruments* **2012**, 83, 123902.
2. J.-H. Bahk, A. Shakouri, *Physical Review B* **2016**, 93, 165209.
3. M. Thesberg, H. Kosina, N. Neophytou, *Physical Review B* **2017**, 95, 125206.
4. T. Feng, X. Ruan, *Journal of Nanomaterials* **2014**, 2014.
5. O. Hellman, D. A. Broido, *Physical Review B* **2014**, 90, 134309.
6. G. Kresse, J. Hafner, *Physical Review B* **1993**, 47, 558.
7. G. Kresse, J. Furthmüller, *Physical review B* **1996**, 54, 11169.
8. V. Chis, I. Y. Sklyadneva, K. Kokh, V. Volodin, O. Tereshchenko, E. Chulkov, *Physical Review B* **2012**, 86, 174304.
9. X. Chen, D. Parker, D. J. Singh, *Physical Review B* **2013**, 87, 045317.
10. A. Togo, F. Oba, I. Tanaka, *Physical Review B* **2008**, 78, 134106.
11. D. Bessas, I. Sergueev, H.-C. Wille, J. Perßon, D. Ebling, R. Hermann, *Physical Review B* **2012**, 86, 224301.
12. B. Xu, M. T. Agne, T. Feng, T. C. Chasapis, X. Ruan, Y. Zhou, H. Zheng, J. H. Bahk, M. G. Kanatzidis, G. J. Snyder, *Advanced Materials* **2017**, 29.
13. D. Spitzer, *Journal of Physics and chemistry of Solids* **1970**, 31, 19.
14. S.-i. Tamura, *Physical Review B* **1983**, 27, 858.

15. J. Garg, N. Bonini, B. Kozinsky, N. Marzari, *Physical review letters* **2011**, 106, 045901.
16. W. Kamitakahara, B. Brockhouse, *Physical Review B* **1974**, 10, 1200.
17. L. Lindsay, D. Broido, T. Reinecke, *Physical review letters* **2012**, 109, 095901.
18. T. Feng, B. Qiu, X. Ruan, *Physical Review B* **2015**, 92, 235206.
19. W. Kim, A. Majumdar, *Journal of Applied Physics* **2006**, 99, 084306.
20. N. Mingo, D. Hauser, N. Kobayashi, M. Plissonnier, A. Shakouri, *Nano letters* **2009**, 9, 711.
21. H. Zhang, A. J. Minnich, *Scientific reports* **2015**, 5, 8995.
22. A. Kundu, N. Mingo, D. Broido, D. Stewart, *Physical Review B* **2011**, 84, 125426.